Journal of Power Sources 473 (2020) 228600

Contents lists available at ScienceDirect

Journal of Power Sources

journal homepage: www.elsevier.com/locate/jpowsour

Multiscale 3D hybrid carbon microelectrodes with candle soot and reduced GO nanoparticles as binder-free anode: An approach beyond 3D for high rate & high performance Li-ion batteries

Suresh Mamidi, Anil Daliprasad Pathak, Ananya Gangadharan, Chandra Shekhar Sharma *

Creative & Advanced Research Based on Nanomaterials (CARBON) Laboratory, Department of Chemical Engineering, Indian Institute of Technology Hyderabad, Kandi, 502285, Telangana, India

HIGHLIGHTS

- Hierarchical electrodes are fabricated on SS wafer via the CMEMS and drop casting.
- Hierarchical electrodes exhibited enhanced electrochemical performance.
- GHE and CHE deliver capacities of 549 and 462 $mAhg^{-1}$ at 250 mAg^{-1} after 100 cycles.
- Post cycling analysis confirms the structural integrity of the electrodes.
- Finite element method is used to investigate time-dependent Li-ion gradients.

GRAPHICAL ABSTRACT

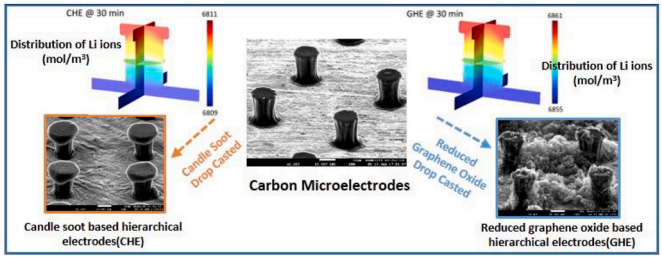

ARTICLE INFO

Keywords:
Hierarchical 3D microelectrodes
Carbon-MEMS
Candle soot
Reduced graphene oxide
Lithium-ion battery

ABSTRACT

The full potential of electrodes for superior electrochemical performance in lithium-ion batteries (LIB) is beyond the limits of conventional planar electrodes with higher mass loadings. In this article, we report a unique way to fabricate a hierarchical hybrid 3D microelectrodes architecture with low mass loading (~1.3 mg/cm^2) for more effective and efficient lithium charge transport in LIB. To fabricate such hierarchical 3D microelectrodes, first, 3D carbon microelectrodes are prepared on stainless steel (SS) wafer via the carbon-MEMS approach followed by drop-casting reduced graphene oxide (rGO) nanoflakes and candle soot carbon nanoparticles solution on these 3D microelectrodes. As-fabricated hierarchical 3D microelectrodes are then tested as an anode in LIB that enabled high current density operations with enhanced specific capacities. 3D carbon hierarchical microelectrodes based on rGO and candle soot carbon nanoparticles with SS substrate deliver high specific capacities of 560 and 462 $mAhg^{-1}$ at 250 mAg^{-1} current density after 100 cycles, respectively. Post cycling analysis after 100 cycles confirms the structural integrity of the electrodes. Further, the finite element method is used to investigate and predict the time-dependent Li-ion gradient within the 3D microelectrodes that confirms much improved Li-ion diffusion kinetics over conventional flat electrodes.

* Corresponding author.
E-mail address: cssharma@che.iith.ac.in (C.S. Sharma).

https://doi.org/10.1016/j.jpowsour.2020.228600
Received 27 March 2020; Received in revised form 15 June 2020; Accepted 30 June 2020
Available online 21 July 2020
0378-7753/© 2020 Elsevier B.V. All rights reserved.

1. Introduction

Lithium-Ion batteries (LIB) are one of the potential energy storage devices that are used in a wide range of applications, from miniaturized devices to high power-driven electric vehicles [1,2]. In electric vehicle requirements, LIB has to deliver high energy and power density. It is a fact that the electrochemical performance and stability of a LIB is majorly dependent on active electrode materials used in the assembly/fabrication process. Hence, the design and material aspects of electrodes have become an exciting area for the scientific community to achieve high energy and power densities.

In the anode materials perspective, commercially available graphite is used in conventional LIB. Graphite as an anode is highly successful due to its excellent cyclic stability but suffers serious limitations like low theoretical capacity (372 $mAhg^{-1}$) and poor rate capability. Many new carbon materials such as reduced graphene oxide (rGO), carbon nanotubes, fullerenes and candle soot (CS) have been reported as a substitute to graphite in LIB [3–6]. Among these carbon materials, rGO and CS stand in frontline that delivers high rate performance with excellent cyclic stability.

rGO is a monolayer of sp^2 hybridized carbon atoms closely packed into a two-dimensional (2D) honeycomb lattice. Fabrication methods like dip coating, spin coating, self-assembly and spray coating are used to prepare rGO thin films [7–11]. Several reports reveal the use of these rGO films in the fabrication of supercapacitors, solar cells, and transparent conductive films [12–14]. The intrinsic low electrical resistivity and high surface area of rGO results in outstanding performance when tested as an anode in LIB [15,16].

CS is synthesized by uncontrolled combustion of wax, which is known as a flame synthesis method [17,18]. CS has fractal-like structures where carbon nanoparticles (CNP) are interconnected and used in several applications like energy storage devices, low-cost detectors, solar cells and hydrophobic coatings [19–24]. It has shown an ultra-high rate performance when tested as an anode in LIB delivering capacity of 170 mAh/g at 10 C-rate, which is comparable to commercially used expensive electrodes [6,25]. Thereby, CS has become an inexpensive and effective source of carbon that can be used in energy storage devices. Further other carbon materials such as hard carbon-transition metal oxide, polymer coated metal oxide composites, metal-multi walled carbon nanotubes composites are also used for improved electrochemical performance [26–29].

In the design aspects, 3D microelectrodes offer significant advantages over planar electrodes such as (i) large surface area electrodes (ii) short diffusion lengths when compared to conventional electrodes (iii) large specific capacities for the same foot print area and (iv) fast charge-discharge kinetics [30–33]. The fabrication of 3D carbon pillars and hierarchical electrodes is a step laid towards miniaturization of battery with smaller dimensions that can achieve large storage capacities and deliver high energy densities. 3D carbon microelectrodes fabricated on Silicon (Si) wafer has shown 80% more specific capacity in the same areal footprint of carbon thin film (CTF) [31]. Furthermore, efforts have been made to improve the electrochemical performance of the cell by replacing Si with Stainless steel (SS) substrate due to its high electrical conductivity [34,35]. These 3D microelectrodes are fabricated via microelectronics and mechanical system (MEMS) technique with SU-8 as a base material. SU-8 is a negative tone photoresist whose properties are amplified with exposure of UV rays. Initially, SU-8 microstructures are fabricated and then skillfully pyrolyzed to get 3D carbon microelectrodes on the SS substrate. Such 3D carbon microelectrodes have yielded a specific capacity of 592 $mAhg^{-1}$ at 37.2 mAg^{-1} current density [35]. However, the cyclic stability of the cell devastated gradually due to trapping of Li-ions in the inner pores of the electrodes and Li plating [36] at empty spaces of the SS current collector, resulting in high irreversible capacity over subsequent cycles. In order to resolve these two critical issues, a novel hybrid electrode configuration of conductive rGO and inexpensive CS decorated around 3D carbon microelectrodes are reported here.

In this work, CS and rGO are synthesized using facile flame synthesis and modified Hummer's method, respectively [6,37]. Later on, these materials are integrated with 3D carbon microelectrode to fabricate hybrid and hierarchical electrodes via a simple drop-casting method. The current method avoids the usage of any safety hazards such as flammable N-Methyl-2-pyrrolidone (NMP) solvent and Polyvinylidene fluoride (PVDF) binder. It is known that the PVDF reacts with lithiated carbon at elevated temperatures, which are exothermic reactions, which eventually leads to an explosion [38]. Moreover, the drop casting approach is a facile and an inexpensive technique when compared to the other deposition techniques like electrospraying, spin coating and chemical vapor deposition [34,39,40]. As prepared samples are characterized physically and structurally using field emission scanning electron microscope (FESEM) and Raman spectroscopy, respectively. Further, these hybrid and hierarchical electrodes are electrochemically characterized using them as an anode in LIB. To investigate further, finite element based COMSOL Multiphysics simulation is performed to analyze the ease of Li-ion diffusion across the 3D microelectrodes and Li-ion charge transport kinetics is compared with 2-D flat electrodes.

2. Experimental

2.1. Design

The dimensions of the 3D carbon microelectrodes are predetermined based on Li-ion penetration depth to improve the electrochemical performance by utilizing microelectrode volume effectively. The average diameter and height of the cylindrical carbon micro-posts are maintained as 14 and 20 μm, respectively.

2.2. Fabrication of 3D carbon microelectrodes

A well-reported carbon-MEMS (C-MEMS) fabrication technique is deployed to synthesize the carbon microelectrodes on SS current collector. Initially, SU-8 2050 (Make: MicroChem) is spin-coated on a SS substrate (Make: MTI Corp, 304 Grade) at 3000 rpm for 30 s to get a film thickness of 50 μm. Later, this film is pre-baked at 65 °C and 95 °C for 2 and 5 min, respectively. The pre-baked photoresist film is kept under a chrome mask (Make: Front Range) of 20 μm diameter and 40 μm spacing and exposed to UV rays ($\lambda = 365$ nm) for 20 s to promote cross-linking in the photoresist film. Furthermore, the rate of the cross-linking reaction enhanced by baking the post-exposure film at 65 and 95 °C for 1 and 6 min, respectively. Such films are transferred to the developer solution (Make: MicroChem) for removal of the unexposed parts of the photoresist film to yield uniform SU-8 microstructures. These SU-8 microstructures are placed on a hotplate to bake them at 150 °C for 5 min, which helps in relieving the residual stresses involved in microstructures. Finally, these SU-8 microstructures were pyrolyzed at 900 °C for 60 min in a tubular furnace (Make: Carbolite Zero) under argon atmosphere. During pyrolysis, the optimized gas flow rate was maintained to retain the morphology of microstructures on the substrate.

2.3. Candle soot drop-casted 3D carbon microelectrodes

By simple flame synthesis as reported earlier [6], 0.5 mg of CS is collected at the tip of the candle flame and dispersed in 0.5 ml ethanol. The as-prepared solution is sonicated for 10 min for uniform dispersion. This solution is then drop-casted onto 3D carbon microelectrodes that are placed on a hot plate at 100 °C. As the set temperature is higher than the ethanol boiling point at atmospheric pressure, the solvent instantaneously vaporizes, leaving decorated CS over the 3D microelectrodes array. This facile way also allows us to deposit CS in empty spaces on the substrate and all over the microelectrodes array. CS deposited hybrid microelectrodes are denoted as CHE.

2.4. rGO drop-casted hybrid microelectrodes

The rGO is synthesized from graphite flakes via modified hummer's method [37]. 0.5 mg of rGO is dispersed in 0.5 ml of ethanol and sonicated for 10 min to obtain a uniform dispersion. Similar to the fabrication of CHE, the rGO dispersed solution is drop-casted on 3D microelectrodes placed on the hot plate at 100 °C. As fabricated hybrid electrodes with rGO drop-casted on 3D carbon microelectrodes are designated as GHE.

2.5. Structural characterization

FESEM (Make: JEOL, Model: 2100), TEM (Make: FEI Tecnai, Model: G2S-Twin) and Optical profiler (Make: Aep-technologies, Model: Nanomap-D), were used to study the surface morphology and depth profile analysis for SU-8, carbon, and hybrid electrode microarrays, respectively. X-ray diffraction (Make: PANalytical, Model: X'Pert PRO) and Raman spectroscopy (Make: WITec, Model: alpha300) was used to investigate the crystallinity of the different materials available in hybrid electrodes.

2.6. Electrochemical tests

As prepared, CHE and GHE on stainless steel (Grade 304) current collector were used as working electrodes, whereas lithium foil is used as a counter and reference electrodes in the coin cell assembly (CR 2032). The mass loading of 3D microelectrodes is on bare SS current collector is ~1 mg/cm^2. In case of CHE and GHE, additional active material in the form of CS and rGO is provided, respectively, which increased the mass loading to 1.3 mg/cm^2 (30% more mass loading). 1 M $LiPF_6$ dissolved in ethylene carbonate and dimethyl carbonate in 1:1 (w/w) is used as an electrolyte (amount: 100 μL) with which Whatman glass microfibers separator (thickness: 0.67 mm) is soaked and used between working and counter electrode. These coin cells are packed in a controlled argon atmosphere chamber (Glovebox, Make: MBRAUN) with oxygen and moisture levels less than 0.1 ppm. Electrochemical impedance spectroscopy (EIS), cyclic voltammetry (CV) and galvanostatic charge-discharge (GCD) experiments are performed using the potentiostat (Make: Biologic Instruments, Model: VSP-300). CV and GCD measurements are performed in the voltage range of 0.01–3 V. EIS analysis are carried out in the frequency range of 0.1Hz to 1 MHz.

3. Results and discussion

3.1. Structural characterization

A combination of CMEMS followed by simple drop-casting techniques is used to fabricate hierarchical 3D electrodes that inspect the material and design aspect of electrodes as illustrated in Fig. 1. Initially, in the design aspect, SU-8 microstructures are patterned on SS current collector via photolithography method in which process parameters such as pre-exposure bake time, exposure dosage, post-exposure bake and developing time are optimized. These parameters are firmly responsible for the proper adhesion of SU-8 microarrays to the substrate. After a successful attempt, the 3D view of SU-8 microstructures can be seen in Fig. 2a. These microstructures are then carbonized in the tubular furnace with controlled argon gas flow rates and optimum temperature profiles to yield 3D carbon microelectrodes as shown in Fig. 2b. Conventionally, Si substrate is used as a base to fabricate SU-8 microstructures due to its excellent adhesion capability [32,41]. However, the use of Si as a current collector in LIB is impractical due to its high electrical resistivity. Therefore, we replaced the conventional Si with SS current collector as discussed in one of our previous works [35]. This opens up a wide window of research for micro batteries that can impact miniaturized electronics to a greater extent. After the successful fabrication of 3D carbon microelectrodes on SS, the electroactive surface area of these microelectrodes array is further improved by fabricating multiscale hybrid electrodes using an inexpensive drop-casting method. Further, CS nanoparticles and rGO nanoflakes are dispersed in ethanol separately and drop-casted on carbon microelectrodes to synthesize CHE and GHE, respectively. The key features of the hybrid electrodes are that they possess a unique morphology, multiscale interconnected nanostructures with the high surface area. These hybrid electrodes provide numerous active sites for Li-ion intercalation along with a continuous conducting path for electron transfer.

Optical profiler (Fig. 2a) displayed the SU-8 microstructures with 50 μm height, 25 μm diameter, and 30 μm spacing. Further, post-pyrolysis carbon microelectrodes are shown in Fig. 2b. From the profilometry, the primary observation is that the microstructures are intact to the substrate after the pyrolysis. The inevitable dimensional changes are observed for SU-8 microstructures upon pyrolysis, resulting from the near isotropic shrinkage and leave carbon microelectrodes with 20 μm height, 14 μm diameter and 40 μm spacing. A similar geometry dimension is used to simulate the Li-ion diffusion over the carbon microelectrodes (section 3.4). Fig. 2c and d depicted the presence of 3D hierarchical hybrid electrodes, interconnected CS nanoparticles, and

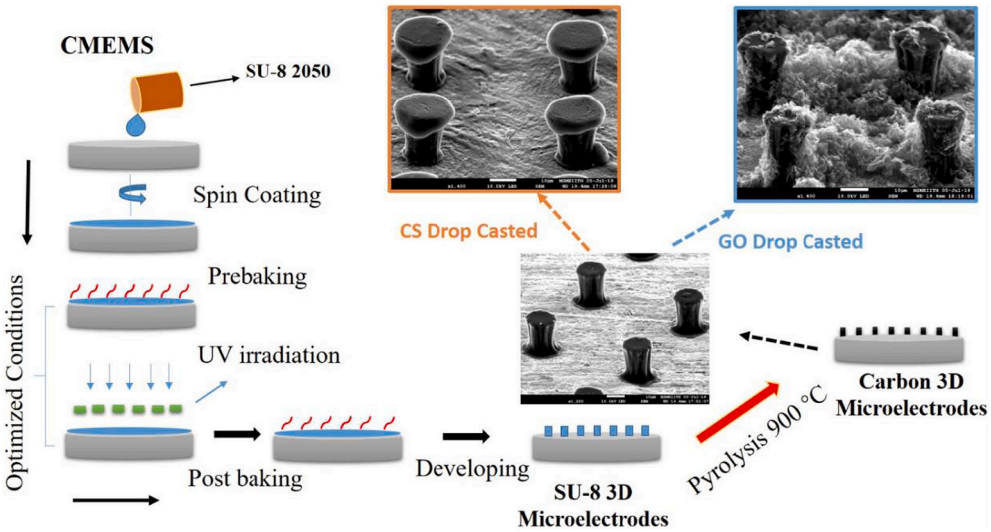

Fig. 1. Schematic for preparing 3D hierarchical hybrid microelectrodes.

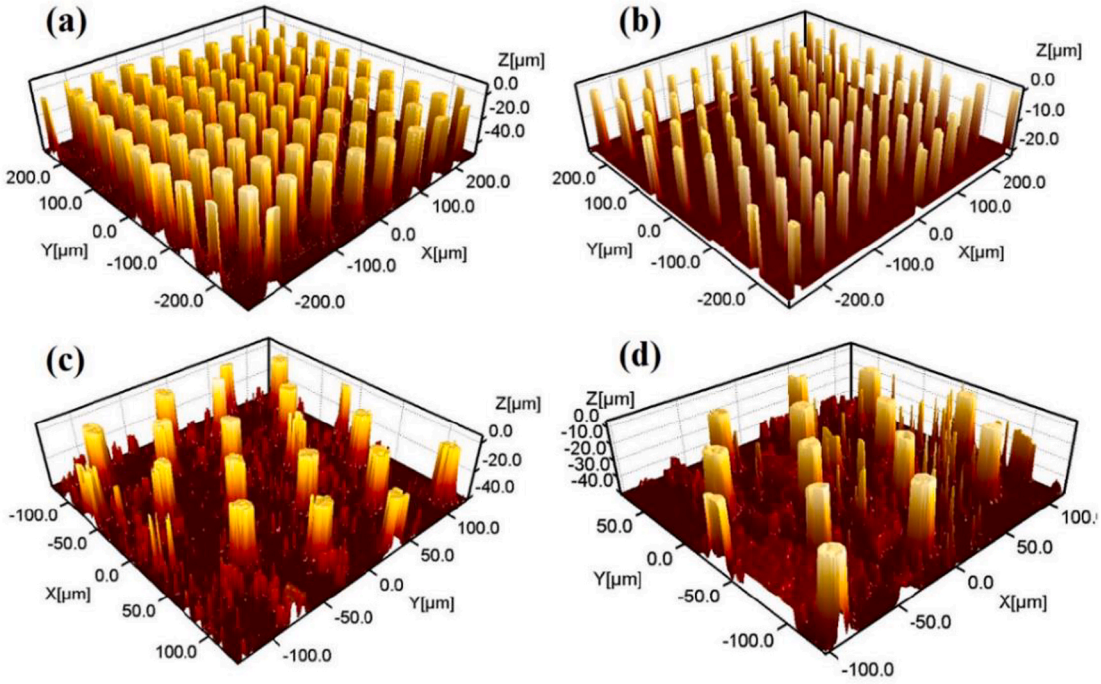

Fig. 2. Optical profiler images of (a) SU-8 3D microstructures on SS. (b) 3D carbon microstructures on SS (c) candle soot and (d) rGO based 3D hybrid structures, CHE and GHE.

rGO nanoflakes in between the pillars of CHE and GHE, respectively.

For a better understanding of the structures, FESEM imaging is also done. Fig. 3a–f illustrates the FESEM micrographs of carbon microelectrodes and hierarchical microelectrodes. Fig. 3a–b shows only 3D carbon microelectrode arrays at different magnification. Fig. 3c–d shows CS-based 3D hybrid electrode. As mentioned earlier, the unique form of mushroom topology was exhibited by CHE (Fig. 3c) due to the instant vaporization of ethanol solvent during heat treatment in the drop-casting. From the TEM image of CS (Fig. S1), it can be observed that the CS nanoparticles are highly interconnected and formed a fractal-like network. Primarily, the CS nanoparticles are in a spherical shape with an approximate average diameter of 40 nm.

Fig. 3e and f show the interconnected CS nanoparticles are available in the spaces and as well as on microelectrodes. Therefore, we could fabricate a multiscale hybrid high surface area electrode using this combinatorial way. Fig. 3g and h show that the 3D carbon microelectrodes are surrounded by high surface area rGO nanoflakes. From the high magnification image (Fig. 3h), it is observed that feathery rGO nanoflakes are well decorated around 3D carbon microelectrodes upon drop-casting. These rGO nanoflakes are also largely interconnected which may improve the electrical conductivity among the 3D microelectrodes during the electrochemical activities.

As the microstructure of electrode plays a key role in electrochemical performance, X-ray diffraction patterns of rGO, CS and SU-8 derived 3D carbon microstructures were analyzed and presented in Fig. S2. The two characteristic diffraction peaks at 24.5° and 43° indicates the (002) and (100) planes of the hexagonal structure of carbon, respectively [42]. We have calculated the interlayer spacing (d_{002}) between graphene layers from the corresponding peak positions of (002) plane using Bragg's equation [43]. The inter-planar spacing of rGO, CS and SU-8 derived 3-D carbon microstructures are 0.35, 0.34 and 0.36 nm, respectively and larger than that of standard graphite (0.335 nm). The larger interlayer distance will provide additional accommodation site for lithium during intercalation and will improve the electrochemical performance [42].

Raman spectra were recorded for CHE and GHE to obtain the defect density, degree of crystallinity and the finite crystallite sizes that are perpendicular to the hexagonal axis. As shown in Fig. 4a and Fig. 4b, Raman spectra were recorded specifically on the top of the pillar and as well as at the base for CHE and GHE. In both cases, the characteristic D-band and G-band are observed at ~1347 cm^{-1} and ~1589 cm^{-1}, respectively. The D-band represents the radial A_{1g} breathing mode of vibration, which, in turn, signifies the disorder content [44]. Similarly, the G-band is observed due to in-plane E_{2g} vibrations corresponding to crystalline sp^2 domains [44–47]. Therefore, the intensity ratio (I_D/I_G) is widely used to trace the defect quantity in the probed material.

From Fig. 4a and b, a difference in I_D/I_G of pillars is noticed which can be due to CS nanoparticles are uniformly distributed on the pillar and base for CHE, whereas rGO is spread only at the base of GHE but not on the pillars. From this, it is evident that CS material filled the gap between pillars completely making these as high surface area electrodes array apart from being multiscale in nature. The I_D/I_G ratio for CS and rGO at the base is found to be 0.83 and 0.99, respectively. It can be observed that rGO at base of GHE electrode has higher I_D/I_G ratio compared to CS, indicating substantial degree of disorder/defect density. The higher degree of disorder in GHE electrode will further help to improve the electrochemical performance as discussed in section 3.2. The additional peaks (including 2D, and combined (D + G)) are recorded in the range 2500–2800 cm^{-1} which is mostly arise from the all kinds of sp^2 carbon materials, this indicates the second-order two-phonon process associated with defects present in the graphitic structure of the carbon material [48]. The in-planar crystallite thickness perpendicular to the hexagonal axis of CHE and GHE were calculated using the empirical formula $L_a = 4.4(I_G/I_D)$ [44,48]. The crystallite thickness found to be 5.3 nm and 4.4 nm for base and 5.1 nm and 4.9 nm for top of pillar. The values are tabulated (Table S1) and correlated with the electrochemical performance of the battery (section 3.2).

3.2. Electrochemical performance

The electrochemical properties of CHE and GHE are evaluated as an anode in half-cell configuration mode using CV, GCD and EIS measurements. Fig. 5a depicts the comparative plot of first cycle CV measurement for CHE, GHE, CS and rGO at 0.1 mVs^{-1}. The capacity loss in the first cycle corresponding to the solid electrolyte interphase (SEI)

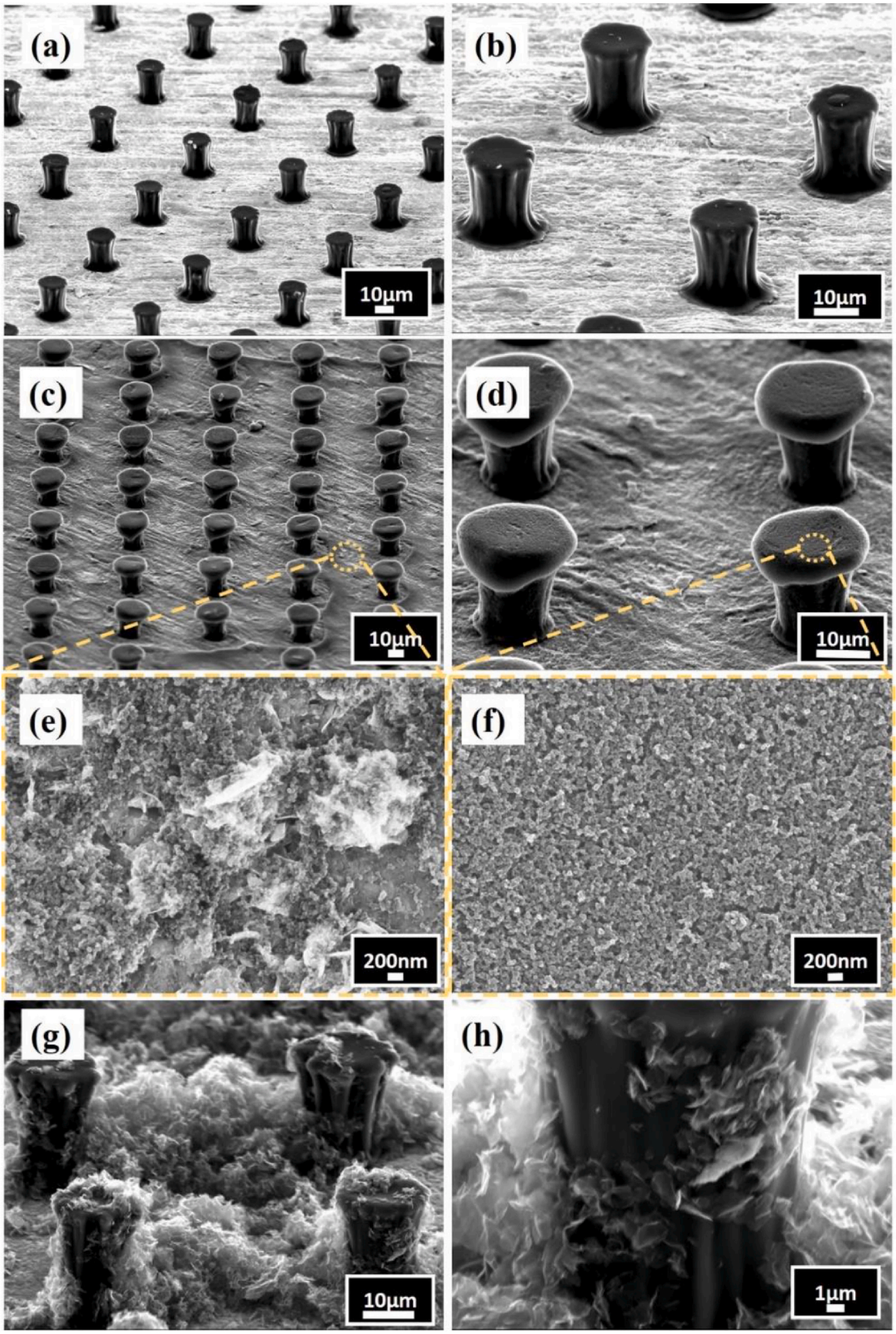

Fig. 3. FESEM image of (a) 3D carbon microstructures on SS. (b) High magnification image of 3D carbon microstructures on SS. (c) CHE. (d) High magnification image of CHE. (e) High magnification image of CNP on base. (f) High magnification image of CNP on pillar. (g) GHE. (h) High magnification image of GHE.

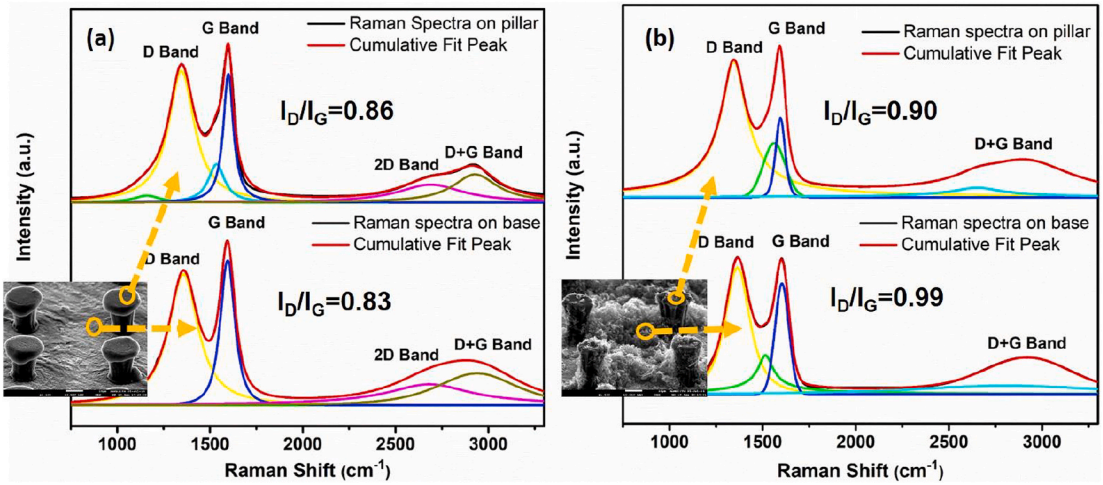

Fig. 4. Raman Spectra of (a) CHE on top of carbon micropillar and CNP coated substrate. (b) GHE on top of carbon micropillar and rGO coated substrate.

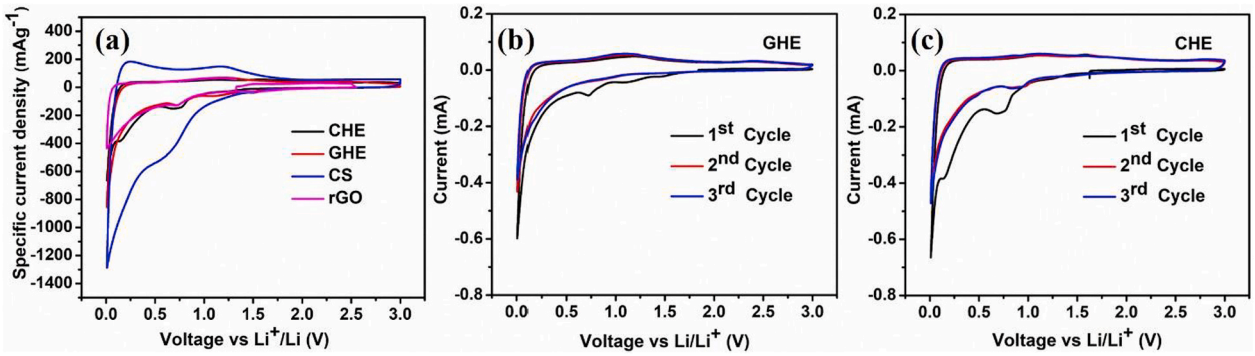

Fig. 5. (a) Comparative plot of first cycle CV measurement for CHE, GHE, CS and rGO at 0.1 mVs^{-1}. (b and c) CV measurement of GHE and CHE in 0–3 V potential window.

formation is highest in case of CS compared to the other systems [49]. Fig. 5b and c illustrate the initial 3 cycles of CV of GHE and CHE, respectively. Comparison of the peaks corresponding to insertion reaction in the first and subsequent cycles reveal that CHE has significant irreversible capacity loss than that of GHE. The higher irreversible capacity loss in case of CHE can be attributed to the functional groups attached to the candle soot CNP [6] that leads to loss of Li-ions through side reactions. From the CV (Fig. 5a, b and c), peak at 0.73V (1st cycle) is due to the electrolyte decomposition and simultaneous SEI formation. In the subsequent cycles, this peak disappears supporting the formation of a stable SEI layer. For 3D microelectrodes on bare SS, the unstable SEI and lithium plating has led to a poor cyclic stability of the cell [35]. However, in the present work, the unwanted lithium-plating problem is addressed by depositing carbon nanostructures (nanoflakes or nanoparticles) at the base of 3D microelectrodes. Besides, there are other methods also such as electrolyte additives, usage of 3D current collectors and multifunctional protective layers to suppress this lithium plating or dentrites formation [50–52].

In case CHE and GHE, the cathodic and anodic peaks near 0.01 V are due to the Li adsorption and desorption at both sides of graphene layers. These observations are in accordance with previously reported hard carbon-based anodes [53].

Fig. 6a represents the first cycle GCD profiles of CHE and GHE at 37.2 mAg^{-1} current density. CHE exhibited discharge and charge capacities of 695 and 590 mAhg^{-1}, respectively, whereas GHE showed a discharge and charge capacities of 777 and 713 mAhg^{-1}, respectively. The high reversible capacity of GHE when compared to CHE can be correlated to the Raman studies as described in Table S1. The presence of rGO nanoflakes in GHE electrode increase the degree of disorder (i.e. I_D/I_G ratio) which implies that the accommodation sites for Li-ion insertion/de-insertions are more in GHE when compared to CHE. Therefore, the obtained initial specific capacity for GHE (777 mAhg^{-1}) is more compare to CHE (695 mAhg^{-1}).

Not only the initial specific capacity is high for GHE than CHE but also the first cycle irreversible capacity loss is lower for GHE (60 mAhg^{-1}) than CHE (105 mAhg^{-1}). The initial coulombic losses attribute to the irreversible consumption of Li-ions and subsequent formation of SEI. A small plateau is also observed at 0.7V for GCD profiles that depicts the onset of SEI formation and also correlates with CV measurements. The capacity enhancement and reversibility of GHE when compared to CHE can be due to the presence of high surface area and electrical conductivity as well as rGO nanoflakes that interconnected with the 3D microstructures. Moreover, CS contains aromatic C–H, carboxyl (C–O) and hydroxyl functional groups while contributes to the irreversible capacity of CHE [6]. Furthermore, the amount of wax embedded in the electrode due to the direct deposition of candle soot on the current collector can also be a reason for the higher irreversible capacity of CHE than GHE [6]. However despite hard carbon nature, the initial coulombic efficiencies for both, CHE and GHE (84.8 and 92.2%, respectively) are significantly high due to the novel architecture of these electrodes.

The rate capability test of CHE (Fig. 6b) are performed at various current densities 37.2, 100, 250, 500, and 1000 mAg^{-1} and the cell exhibited discharge capacities of 645, 551, 466, 356, and 264 mAhg^{-1} respectively. The cell could retain the specific discharge capacity of 640 mAhg^{-1} at 37.2 mAg^{-1} current density with a capacity loss of only 5

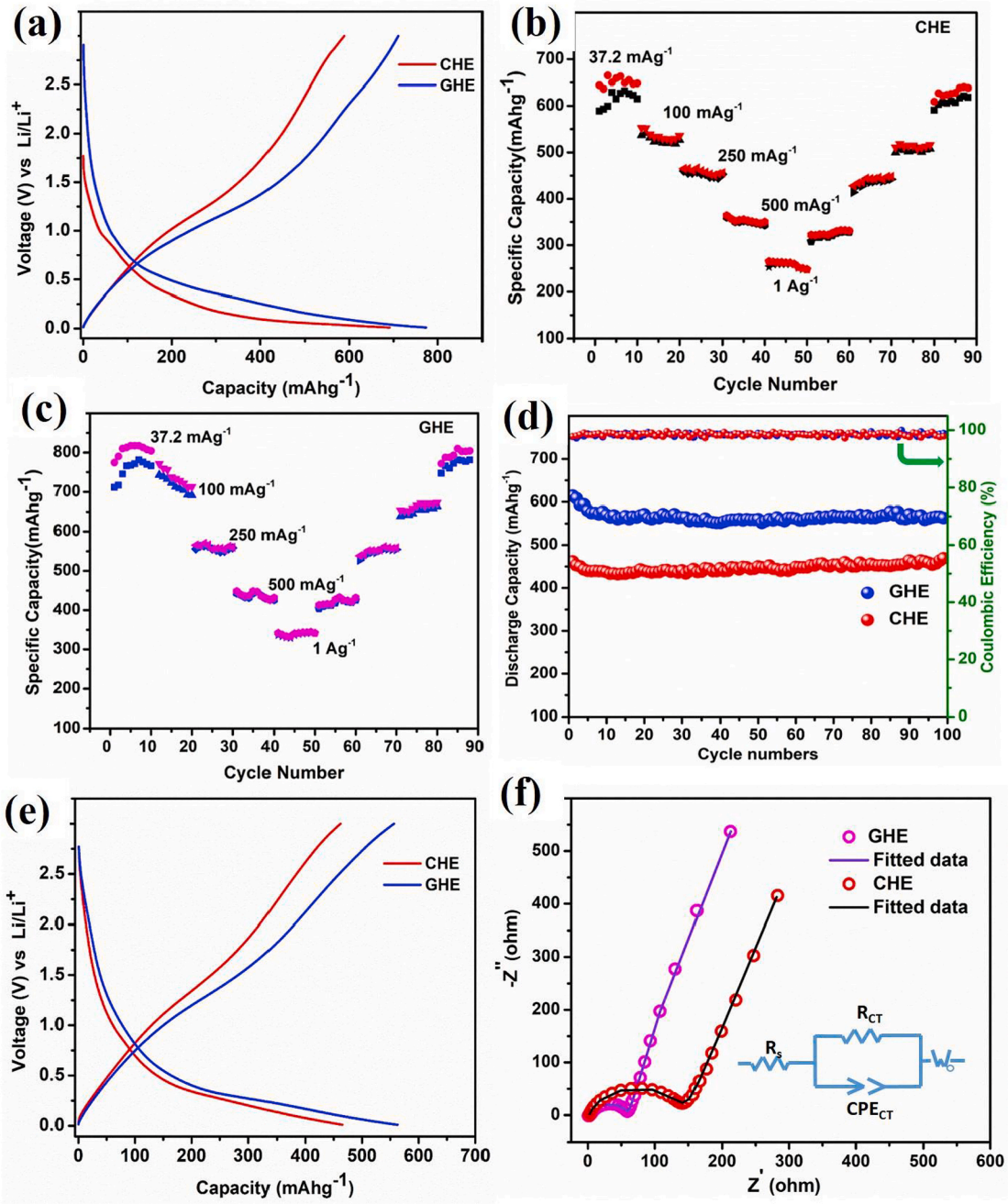

Fig. 6. (a) Comparative GCD profile plot of CHE and GHE at 37.2 mAg^{-1} for first cycle. (b) Rate capability measurement for CHE. (c) Rate capability measurement for GHE. (d) GCD stability plot for CHE and GHE at 250 mAg^{-1} for 100 cycles. (e) Comparative GCD profile plot of CHE and GHE at 250 mAg^{-1} after 100 cycles. (f) The comparative plot of EIS measurement for CHE and GHE from 0.1Hz to 1 MHz.

$mAhg^{-1}$ after the rate capability measurement.

Similarly, GHE has exhibited outstanding discharge capacities of 774, 771, 565, 448 and 341 $mAhg^{-1}$ when tested at 37.2, 100, 250, 500, and 1000 mAg^{-1} current densities respectively (Fig. 6c). The impressive electrochemical performance is mainly due to the existence of multiscale structures. In this GHE configuration, the electrode consists of high surface area carbon microelectrodes along with nanostructured rGO flakes. These rGO nanoflakes are highly electrically conductive and thereby provide efficient electron pathways and interconnectivity among the carbon microelectrodes. The cell has retained a high specific discharge capacity of 771 $mAhg^{-1}$ at 37.2 mAg^{-1} current density with 96.8% coulombic efficiency after rate capability measurement.

Further, the stability test of CHE and GHE has been performed at a high current density of 250 mAg^{-1} for100 cycles (Fig. 6d). The CHE cell exhibited a discharge capacity of 462 $mAhg^{-1}$ after 100 cycles with minimal capacity fade 0.43%. The electrochemical performance is significantly superior than our previously reported material, i.e., only carbon microelectrodes array [35]. The superior performance of CHE when compared to only 3D microelectrodes array is due to (i) the presence of CS carbon nanoparticles that facilitates efficient conductive paths for electrons. (ii) high active material loading (30% more mass loading) and (iii) preventing the direct contact of electrolyte and Li-ions with the current collector thus by suppressing any dead lithium formation. In case of GHE, after 100 cycles of charge-discharge measurements at 250 mAg^{-1} current density the cell retained a discharge capacity of 560 $mAhg^{-1}$ with 98.2% coulombic efficiency and 8.7% capacity fade

(Fig. 6e). Moreover, it is observed that the disorderness and small crystallite size of GHE is favorable for the capacity enhancement, but at the same time, crystallinity of CHE played a vital role in achieving good capacity retention and columbic efficiency. From this cyclic stability of CHE and GHE, it is evident that the Li plating problem of 3D microelectrodes is addressed by preventing any electrolyte contact with the current collector.

To evaluate the electrochemical impedance of the battery EIS measurement of CHE and GHE has been carried out in the frequency range (0.1Hz - 1 MHz) shown in Fig. 6f. The obtained EIS data are fitted with an equivalent circuit that consists of resistors, constant phase element and Warburg diffusion coefficient in series and parallel combinations, as shown in Fig. 6f. Rs indicates the series resistance, which is due to electrolyte solution resistance [54]. For CHE and GHE, Rs is found to be 2.3 and 4.1 Ω, respectively. Whereas the charge transfers resistance, Rct of CHE and GHE are estimated as 127.4 Ω and 54.3 Ω, respectively. The lower Rct of GHE shows the improvement in charge transfer kinetics, which is due to the smaller crystallite size (Table S1) [55]. Also, the presence of insulating candle (paraffin) wax in the CS carbon nanoparticles [6] increases the charge transfer resistance compared to rGO. We have calculated the diffusion coefficient based on electrochemical impedance spectroscopy (EIS) data of the 3D microelectrodes [56]. The calculated diffusion coefficients of Li ions in GHE and CHE microelectrodes are 3.0×10^{-10} m^2/s and 1.0×10^{-10} m^2/s, respectively. This implies that the GHE has better surface contact with the electrolyte with improved lithium ion flux (D_{Li}) compared to CHE [55]. Further, when the hybrid electrodes results are compared to our previous study on only 3D microelectrodes array, the interconnectivity of these microelectrodes array using CS carbon nanoparticles and rGO nanoflakes seems to improve Li-ion intercalation kinetics [35].

3.3. Post-mortem analysis of CHE and GHE microelectrodes after 100 cycles

The microstructural and elemental changes of CHE and GHE microelectrodes are observed by FESEM and EDAX analysis after 100 cycles to investigate the dimensional stability of 3D microelectrode over the cycling. The coin cells are de-crimped after 100 galvanostatic charge-discharge cycles. Fig. 7a and b shows the FESEM image of CHE and GHE at a 60° tilt angle after the 100 cycles. The elemental EDAX analysis of CHE and GHE summarized in Fig. 7(i–v) and Fig. 7(vi-x). The elemental mapping indicates that the carbon and oxygen are uniformly distributed all over the electrodes whereas silicon (with oxygen) is only present in the glass micro filter fibers (separator) attached to the electrodes. It is evident that the morphology of the hybrid structures is retained after cycling and most importantly, the structures remain intact to the substrate. Therefore, this novel hierarchical electrode configuration has great potential in terms of the electrochemical and structural performance of the LIB.

3.4. Diffusion model for 3D microelectrodes

A three-dimensional diffusion-limited model is developed to investigate the time-dependent distribution of Li ions through 3D hierarchical electrodes. The finite element method (FEM) is deployed to construct the diffusion model using COMSOL multiphysics simulation platform. Further, the model is used to analyze the effect of 3D microelectrodes architectures over the flat shape electrode configuration on the electrochemical performance. The movement of lithium-ion in the electrode is considered due to the concentration gradient and is described by the Fick's second law of diffusion neglecting the migration and reaction source term effects as:

$$\frac{\partial c_{Li}}{\partial t} = \nabla \bullet (D_{Li} \nabla c_{Li})$$

Where D_{Li} is the diffusion coefficient (m^2/s) of Li-ion in 3D microelectrodes. C_{Li} is the concentration of Li-ion (mol/m^3). This FEM model is applied to the 3D microelectrodes and an attempt is made to replicate the exact physical size and structure of the microelectrode, according to the optical profiler image (Fig. 2). The average diameter and height of the cylindrical carbon 3D microelectrodes are considered as 14 and 20 μm, respectively as shown in Fig. 8a. To have the exact experimental condition of the simulated model, we applied the experimentally calculated flux boundary condition based on applied current density as:

$$D_{Li} \frac{\partial c_{Li}}{\partial x} = -\frac{i_{app}}{nF}$$

where i_{app} is the applied current density (A/m^2), F is Faraday constant 96485 C/mol and n is the number of electrons involved in the reaction. The calculated diffusion coefficient (D_{Li}) of Li ions in GHE and CHE microelectrodes are considered. Fig. 8b and c shows the lithium distribution over the GHE and CHE after 30 min, respectively. The lithium distribution in both cases is not much varied because the diffusion in the 3D micro carbon pillar is dominating over the rGO and carbon soot.

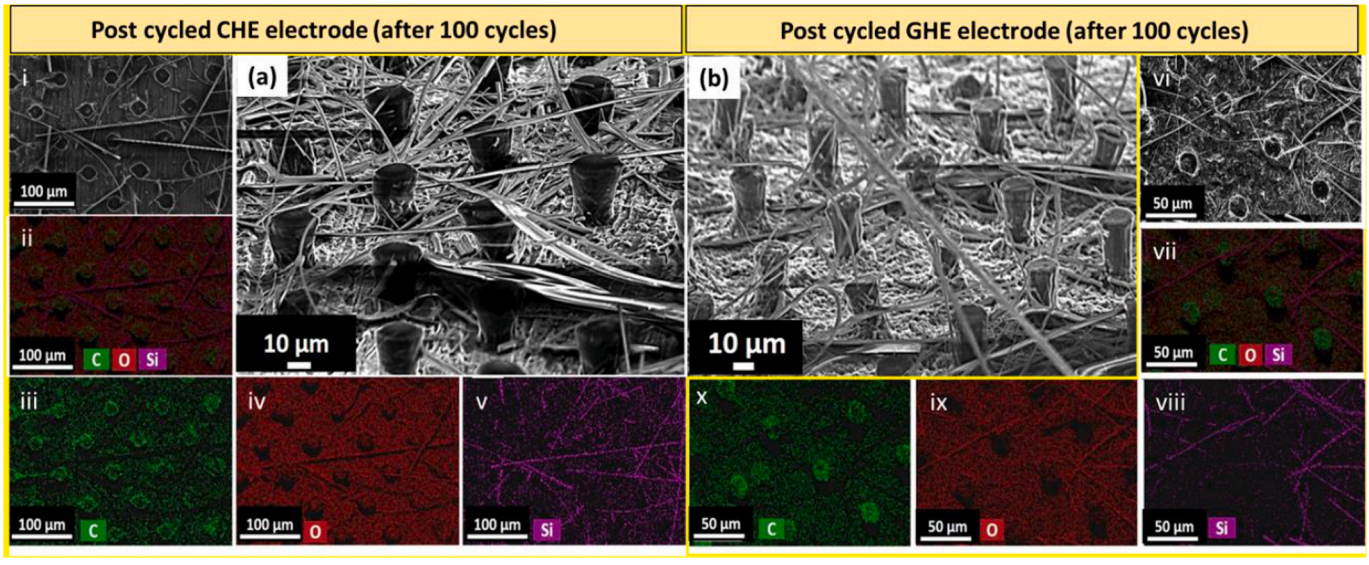

Fig. 7. (a) FESEM micrograph of post cycled CHE at 60° tilt angle; (i–v) EDAX analysis of CHE without tilt angle, (b) FESEM micrograph of post-cycled GHE at 60° tilt angle; (vi-x) EDAX analysis of GHE without tilt angle.

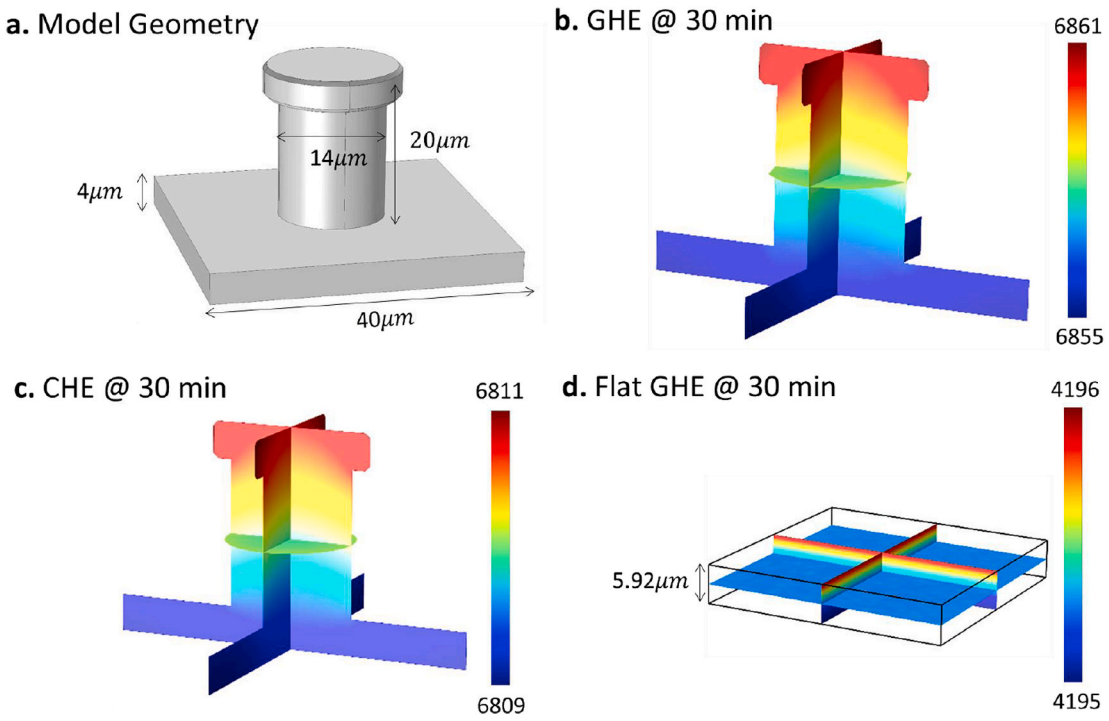

Fig. 8. (a) The geometry dimension used to model and represent the 3D microelectrodes; distribution of Li ions (mol/m^3) through 3D microelectrodes after 30 min for (b) GHE. (c) CHE. (d) 3D micro-flat electrode of GHE.

However, the GHE have shown a better electrochemical performance than CHE this is due to the low electrical resistivity and high surface area of rGO [57,58]. Further, the FEM simulation is performed on the equivalent volume of flat shape electrode to quantify the advantage of 3D carbon microelectrodes over the current flat electrode. Fig. 8d shows the Li-ion distribution over the micro-flat electrode is having a maximum Li-ion concentration of 4196 mol/m^3 compared to the 6861 mol/m^3 for GHE after 30 min. This clearly shows that the advantage of having 3D hierarchical electrodes that provide the effective diffusion of Li-ions, which is near about ~63% over the flat shape electrodes.

4. Summary

The present study successfully demonstrates the fabrication of binder-free multiscale 3D hybrid electrodes that has shown superior electrode capabilities to deliver a high-performance LIB. The fabrication method avoids the use of any hazardous chemicals like flammable NMP solvent and PVDF binder. The unique morphology of the fabricated hybrid electrodes is well studied using optical profiler and FESEM. The correlation behind superior electrochemical performance and morphology is thoroughly studied. Both CHE and GHE retained a capacity of 462 and 560 mAhg^{-1} after 100 cycles of GCD at 250 mAg^{-1} current density. The excellent capacity and structural retention at high current density with enhanced Li-ion storage capabilities make these hybrid electrodes as an outstanding choice to power up the high-performance LIB. Further, the advantage of the novel hierarchical electrode configuration over flat thin-film electrodes is clearly shown using kinetic diffusion studies. Therefore, this work paves the way for next-generation miniaturized LIB that can deliver the high energy and power densities.

Data availability statement

The raw/processed data required to reproduce these findings cannot be shared at this time as the data also forms part of an ongoing study.

Declaration of competing interest

The authors declare that they have no known competing financial interests or personal relationships that could have appeared to influence the work reported in this paper.

CRediT authorship contribution statement

Suresh Mamidi: Methodology, Investigation, Formal analysis, Writing - original draft. **Anil Daliprasad Pathak:** Investigation, Writing - review & editing, Validation. **Ananya Gangadharan:** Investigation, Writing - review & editing. **Chandra Shekhar Sharma:** Conceptualization, Supervision, Writing - review & editing, Resources, Project administration, Funding acquisition.

Acknowledgments

We acknowledge the financial support received from Ministry of Human Resources Development and Department of Heavy Industries, Govt. of India under IMPRINT I scheme (Project 7035) to carry out this work. Mamidi Suresh acknowledges Illa Mani Pujitha for her help in carrying FESEM analysis. Authors are grateful to Darshna Potphode and Shalakha Saha for supplying rGO material.

Appendix A. Supplementary data

Supplementary data to this article can be found online at https://doi.org/10.1016/j.jpowsour.2020.228600.

References

[1] S. Pan, Z. Zhang, W. Weng, H. Lin, Z. Yang, H. Peng, Miniature wire-shaped solar cells, electrochemical capacitors and lithium-ion batteries, Mater. Today 17 (2014) 276–284, https://doi.org/10.1016/J.MATTOD.2014.04.024.

[2] Z.P. Cano, D. Banham, S. Ye, A. Hintennach, J. Lu, M. Fowler, Z. Chen, Batteries and fuel cells for emerging electric vehicle markets, Nat. Energy. 3 (2018) 279–289, https://doi.org/10.1038/s41560-018-0108-1.

[3] E.J. Yoo, J. Kim, E. Hosono, H.S. Zhou, T. Kudo, I. Honma, Large reversible Li storage of graphene nanosheet families for use in rechargeable lithium ion batteries, Nano Lett. 8 (2008) 2277–2282, https://doi.org/10.1021/nl800957b.

[4] B.J. Landi, M.J. Ganter, C.D. Cress, R.A. DiLeo, R.P. Raffaelle, Carbon nanotubes for lithium ion batteries, Energy Environ. Sci. 2 (2009) 638–654, https://doi.org/10.1039/b904116h.

[5] W. Ai, Z. Luo, J. Jiang, J. Zhu, Z. Du, Z. Fan, L. Xie, H. Zhang, W. Huang, T. Yu, Nitrogen and sulfur codoped graphene: multifunctional electrode materials for high-performance LI-ion batteries and oxygen reduction reaction, Adv. Mater. 26 (2014) 6186–6192, https://doi.org/10.1002/adma.201401427.

[6] M. Kakunuri, C.S. Sharma, Candle soot derived fractal-like carbon nanoparticles network as high-rate lithium ion battery anode material, electrochim, Acta 180 (2015) 353–359, https://doi.org/10.1016/j.electacta.2015.08.124.

[7] S.J. An, Y. Zhu, S.H. Lee, M.D. Stoller, T. Emilsson, S. Park, A. Velamakanni, J. An, R.S. Ruoff, Thin film fabrication and simultaneous anodic reduction of deposited graphene oxide platelets by electrophoretic deposition, J. Phys. Chem. Lett. 1 (2010) 1259–1263.

[8] S. Gilje, S. Han, M. Wang, K.L. Wang, R.B. Kaner, A chemical route to graphene for device applications, Nano Lett. 7 (2007) 3394–3398.

[9] J. Peng, W. Gao, B.K. Gupta, Z. Liu, R. Romero-Aburto, L. Ge, L. Song, L. B. Alemany, X. Zhan, G. Gao, Graphene quantum dots derived from carbon fibers, Nano Lett. 12 (2012) 844–849.

[10] X. Wang, L. Zhi, K. Müllen, Transparent, conductive graphene electrodes for dye-sensitized solar cells, Nano Lett. 8 (2008) 323–327.

[11] L. Tang, Y. Wang, Y. Li, H. Feng, J. Lu, J. Li, Preparation, structure, and electrochemical properties of reduced graphene sheet films, Adv. Funct. Mater. 19 (2009) 2782–2789.

[12] S.R.C. Vivekchand, C.S. Rout, K.S. Subrahmanyam, A. Govindaraj, C.N.R. Rao, Graphene-based electrochemical supercapacitors, J. Chem. Sci. 120 (2008) 9–13.

[13] Y. Zhu, S. Murali, M.D. Stoller, K.J. Ganesh, W. Cai, P.J. Ferreira, A. Pirkle, R. M. Wallace, K.A. Cychosz, M. Thommes, Carbon-based supercapacitors produced by activation of graphene, Science 332 (80) (2011) 1537–1541.

[14] J. Zhao, S. Pei, W. Ren, L. Gao, H.-M. Cheng, Efficient preparation of large-area graphene oxide sheets for transparent conductive films, ACS Nano 4 (2010) 5245–5252.

[15] J. Zhang, Z. Xie, W. Li, S. Dong, M. Qu, High-capacity graphene oxide/graphite/carbon nanotube composites for use in Li-ion battery anodes, Carbon N. Y. 74 (2014) 153–162, https://doi.org/10.1016/j.carbon.2014.03.017.

[16] P. Lian, X. Zhu, S. Liang, Z. Li, W. Yang, H. Wang, Large reversible capacity of high quality graphene sheets as an anode material for lithium-ion batteries, Electrochim. Acta 55 (2010) 3909–3914, https://doi.org/10.1016/j.electacta.2010.02.025.

[17] C. Lou, C. Chen, Y. Sun, H. Zhou, Review of soot measurement in hydrocarbon-air flames, Sci. China Technol. Sci. 53 (2010) 2129–2141, https://doi.org/10.1007/s11431-010-3212-4.

[18] A. Gangadharan, S. Mamidi, C.S. Sharma, T.N. Rao, Urea-modified candle soot for enhanced anodic performance for fast-charging lithium-ion battery application, Mater. Today Commun. 23 (2020), 100926, https://doi.org/10.1016/j.mtcomm.2020.100926.

[19] D.D. Potphode, A. Gangadharan, C.S. Sharma, Candle soot carbon as electrode materials for energy storage applications, Proc. Indian Natl. Sci. Acad. (2019), https://doi.org/10.16943/ptinsa/2019/49582.

[20] Z. Zhang, J. Hao, W. Yang, B. Lu, J. Tang, Modifying candle soot with FeP nanoparticles into high-performance and cost-effective catalysts for the electrocatalytic hydrogen evolution reaction, Nanoscale 7 (2015) 4400–4405, https://doi.org/10.1039/c4nr07436j.

[21] M.R. Mulay, A. Chauhan, S. Patel, V. Balakrishnan, A. Halder, R. Vaish, Candle Soot: Journey from a Pollutant to a Functional Material, 2018, https://doi.org/10.1016/j.carbon.2018.12.083.

[22] J. Wei, M. Cai, F. Zhou, W. Liu, Candle soot as particular lubricant additives, Tribol. Lett. 53 (2014) 521–531, https://doi.org/10.1007/s11249-013-0290-z.

[23] X. Deng, L. Mammen, H.J. Butt, D. Vollmer, Candle soot as a template for a transparent robust superamphiphobic coating, Science 335 (80) (2012) 67–70, https://doi.org/10.1126/science.1207115.

[24] B.N. Sahoo, B. Kandasubramanian, An experimental design for the investigation of water repellent property of candle soot particles, Mater. Chem. Phys. 148 (2014) 134–142, https://doi.org/10.1016/j.matchemphys.2014.07.022.

[25] R. Kanakaraj, C. Sudakar, Candle soot carbon nanoparticles as high-performance universal anode for M-ion (M = Li+, Na+ and K+) batteries, J. Power Sources 458 (2020), 228064, https://doi.org/10.1016/j.jpowsour.2020.228064.

[26] H. Qiao, R. Li, Y. Yu, Z. Xia, L. Wang, Q. Wei, K. Chen, Q. Qiao, Fabrication of PANI-coated ZnFe2O4 nanofibers with enhanced electrochemical performance for energy storage, Electrochim. Acta 273 (2018) 282–288, https://doi.org/10.1016/j.electacta.2018.04.010.

[27] A. Gurung, R. Naderi, B. Vaagensmith, G. Varnekar, Z. Zhou, H. Elbohy, Q. Qiao, Tin selenide – multi-walled carbon nanotubes hybrid anodes for high performance lithium-ion batteries, Electrochim. Acta 211 (2016) 720–725, https://doi.org/10.1016/j.electacta.2016.06.065.

[28] M. McGraw, P. Kolla, B. Yao, R. Cook, Q. Quiao, J. Wu, A. Smirnova, One-step solid-state in-situ thermal polymerization of silicon-PEDOT nanocomposites for the application in lithium-ion battery anodes, Polymer 99 (2016) 488–495, https://doi.org/10.1016/j.polymer.2016.05.044.

[29] S. Liu, Y. Liu, W. Lei, X. Zhou, K. Xu, Q. Qiao, W.H. Zhang, Few-layered ReS2 nanosheets vertically aligned on reduced graphene oxide for superior lithium and sodium storage, J. Mater. Chem. A. 6 (2018) 20267–20276, https://doi.org/10.1039/c8ta08206e.

[30] R. Zaouk, B.Y. Park, F. Galobardes, G. Turon, M. Madou, Design and Characterization of 3D Carbon MEMS for Lithium Ion Microbatteries, 2006, pp. 73–76.

[31] G.T. Teixidor, R.B. Zaouk, B.Y. Park, M.J. Madou, Fabrication and characterization of three-dimensional carbon electrodes for lithium-ion batteries, J. Power Sources 183 (2008) 730–740, https://doi.org/10.1016/j.jpowsour.2008.05.065.

[32] C. Wang, G. Jia, L.H. Taherabadi, M.J. Madou, A novel method for the fabrication of high-aspect ratio C-MEMS structures, J. Microelectromechanical Syst. 14 (2005) 348–358.

[33] R.W. Hart, H.S. White, B. Dunn, D.R. Rolison, 3-D microbatteries, electrochem, Commun. Now. 5 (2003) 120–123, https://doi.org/10.1016/S1388-2481(02)00556-8.

[34] M. Kakunuri, C.S. Sharma, Photoresist derived carbon films as high capacity anodes for lithium ion battery, ECS Trans 61 (2014) 37–43, https://doi.org/10.1149/06107.0037ecst.

[35] S. Mamidi, M. Kakunuri, C.S. Sharma, Fabrication of SU-8 derived three-dimensional carbon microelectrodes as high capacity anodes for lithium-ion, ECS Trans 85 (2018) 21–27.

[36] S.S. Zhang, X. Fan, C. Wang, An in-situ enabled lithium metal battery by plating lithium on a copper current collector, Electrochem. Commun. 89 (2018) 23–26, https://doi.org/10.1016/j.elecom.2018.02.011.

[37] D.C. Marcano, D.V. Kosynkin, J.M. Berlin, A. Sinitskii, Z. Sun, A. Slesarev, L. B. Alemany, W. Lu, J.M. Tour, Improved synthesis of graphene oxide, ACS Nano 4 (2010) 4806–4814, https://doi.org/10.1021/nn1006368.

[38] Q. Wang, P. Ping, X. Zhao, G. Chu, J. Sun, C. Chen, Thermal runaway caused fire and explosion of lithium ion battery, J. Power Sources 208 (2012) 210–224.

[39] V. Penmatsa, T. Kim, M. Beidaghi, H. Kawarada, L. Gu, Z. Wang, C. Wang, Three-dimensional graphene nanosheet encrusted carbon micropillar arrays for electrochemical sensing, Nanoscale 4 (2012) 3673, https://doi.org/10.1039/c2nr30161j.

[40] A. Reina, X. Jia, J. Ho, D. Nezich, H. Son, V. Bulovic, M.S. Dresselhaus, J. Kong, Large area, few-layer graphene films on arbitrary substrates by chemical vapor deposition, Nano Lett. 9 (2009) 30–35, https://doi.org/10.1021/nl801827v.

[41] C. Wang, L. Taherabadi, G. Jia, M. Madou, Y. Yeh, B. Dunn, C-MEMS for the manufacture of 3D microbatteries, Electrochem. Solid State Lett. 7 (2004) A435–A438, https://doi.org/10.1149/1.1798151.

[42] B.S. Girgis, Y.M. Temerk, M.M. Gadelrab, I.D. Abdullah, X-ray diffraction patterns of activated carbons prepared under various conditions, Carbon Sci 8 (2007) 95–100, https://doi.org/10.5714/CL.2007.8.2.095.

[43] B. Sakintuna, Y. Yürüm, S. Çetinkaya, Evolution of carbon microstructures during the pyrolysis of Turkish Elbistan Lignite in the temperature range 700-1000°C, Energy Fuel. 18 (2004) 883–888, https://doi.org/10.1021/ef0301809.

[44] J. Schwan, S. Ulrich, V. Batori, H. Ehrhardt, S. r p Silva, Raman spectroscopy on amorphous carbon films, J. Appl. Phys. 80 (1996) 440, https://doi.org/10.1063/1.362745.

[45] F. Tuinstra, J.L. Koenig, Raman spectrum of graphite, J. Chem. Phys. 53 (1970) 1126–1130, https://doi.org/10.1063/1.1674108.

[46] R.J. Nemanich, S.A. Solin, First- and second-order Raman scattering from finite-size crystals of graphite, Phys. Rev. B 20 (1979) 392–401, https://doi.org/10.1103/PhysRevB.20.392.

[47] S. Reich, C. Thomsen, Raman spectroscopy of graphite, Philos. Trans. R. Soc. A Math. Phys. Eng. Sci. 362 (2004) 2271–2288, https://doi.org/10.1098/rsta.2004.1454.

[48] R. Pathak, K. Chen, A. Gurung, K.M. Reza, B. Bahrami, F. Wu, A. Chaudhary, N. Ghimire, B. Zhou, W.H. Zhang, Y. Zhou, Q. Qiao, Ultrathin bilayer of graphite/SiO2 as solid interface for reviving Li metal anode, Adv. Energy Mater. 9 (2019) 1–10, https://doi.org/10.1002/aenm.201901486.

[49] P. Verma, P. Maire, P. Novak, A review of the features and analyses of the solid electrolyte interphase in Li-ion batteries, Electrochim. Acta 55 (2010) 6332–6341, https://doi.org/10.1016/j.electacta.2010.05.072.

[50] R. Pathak, K. Chen, A. Gurung, K.M. Reza, B. Bahrami, J. Pokharel, A. Baniya, W. He, F. Wu, Y. Zhou, K. Xu, Q. Quinn, Qiao, Fluorinated hybrid solid-electrolyte-interphase for dendrite-free lithium deposition, Nat. Commun. 11 (2020) 1–10, https://doi.org/10.1038/s41467-019-13774-2.

[51] K. Chen, R. Pathak, A. Gurung, E.A. Adhamash, B. Bahrami, Q. He, H. Qiao, A. L. Smirnova, J.J. Wu, Q. Qiao, Y. Zhou, Flower-shaped lithium nitride as a protective layer via facile plasma activation for stable lithium metal anodes, Energy Storage Mater 18 (2019) 389–396, https://doi.org/10.1016/j.ensm.2019.02.006.

[52] K. Chen, R. Pathak, A. Gurung, K.M. Reza, N. Ghimire, J. Pokharel, A. Baniya, W. He, J.J. Wu, Q. Qiao, Y. Zhou, A copper-clad lithiophilic current collector for dendrite-free lithium metal anodes, J. Mater. Chem. A. 8 (2020) 1911–1919, https://doi.org/10.1039/c9ta11237e.

[53] J. Yang, X. Zhou, J. Li, Y. Zou, J. Tang, Study of nano-porous hard carbons as anode materials for lithium ion batteries, Mater. Chem. Phys. 135 (2012) 445–450, https://doi.org/10.1016/j.matchemphys.2012.05.006.

[54] Y. Abe, N. Hori, S. Kumagai, Electrochemical impedance spectroscopy on the performance degradation of LiFePO4/graphite lithium-ion battery due to charge-discharge cycling under different c-rates, Energies 12 (2019) 1–14, https://doi.org/10.3390/en12234507.

[55] R. Pathak, A. Gurung, H. Elbohy, K. Chen, K.M. Reza, B. Bahrami, S. Mabrouk, R. Ghimire, M. Hummel, Z. Gu, X. Wang, Y. Wu, Y. Zhou, Q. Qiao, Self-recovery in Li-metal hybrid lithium-ion batteries via WO3 reduction, Nanoscale 10 (2018) 15956–15966, https://doi.org/10.1039/C8NR01507D.

[56] Z.Y. Tang, J.J. Xue, C.Y. Liu, X.G. Zhuang, Determination of the lithium ion diffusion coefficient in graphite anode material, Acta Phys. - Chim. Sin. 17 (2001) 388, https://doi.org/10.3866/PKU.WHXB20010501.
[57] A. Nekahi, P.H. Marashi, D. Haghshenas, Transparent conductive thin film of ultra large reduced graphene oxide monolayers, Appl. Surf. Sci. 295 (2014) 59–65, https://doi.org/10.1016/j.apsusc.2014.01.004.
[58] Y. Zhang, Y. Guo, Y. Wang, T. Peng, Y. Lu, R. Luo, Y. Wang, X. Liu, J.-K. Kim, Y. Luo, Rational design of 3D honeycomb-like SnS2 quantum dots/rGO composites as high-performance anode materials for lithium/sodium-ion batteries, Nanoscale Res. Lett. 13 (2018) 389, https://doi.org/10.1186/s11671-018-2805-x.